

1
2
3
4 **Small-Scale Flux Emergence Observed Using**
5 ***Hinode*/SOT**
6

7
8 **L.M. Thornton · C.E. Parnell**
9

10
11
12 Received: 12 May 2009 / Accepted: 13 October 2010
13 © Springer Science+Business Media B.V. 2010
14

15
16
17 **Abstract** The aim of this paper is to determine the flux emergence rate due to small-scale
18 magnetic features in the quiet Sun using high-resolution *Hinode* SOT NFI data. Small-scale
19 magnetic features are identified in the data using two different feature identification methods
20 (clumping and downhill); then three methods are applied to detect flux emergence events.
21 The distribution of the intranetwork peak emerged fluxes is determined. When combined
22 with previous emergence results, from ephemeral regions to sunspots, the distribution of
23 all fluxes are found to follow a power-law distribution which spans nearly seven orders of
24 magnitude in flux ($10^{16} - 10^{23}$ Mx) and 18 orders of magnitude in frequency. The power-law
25 fit to all these data is of the form
26
27

28
29
$$\frac{dN}{d\Phi} = \frac{n_0}{\Phi_0} \frac{\Phi^{-2.7}}{\Phi_0},$$

30

31 where $\Phi_0 = 10^{16}$ Mx and is used to predict a global flux emergence rate of ≈ 450 Mx cm^{-2}
32 day^{-1} from all features with fluxes of 10^{16} Mx or more. Since the slope of all emerged fluxes
33 is less than -2 , this implies that most of the new flux that is fed into the solar atmosphere
34 is from small-scale emerging events. This suggests that the rate of flux emergence is inde-
35 pendent of the solar cycle and is equivalent to a global rate of flux emergence of more than
36 a few times 10^{25} Mx day^{-1} . The single power-law distribution over all emerged fluxes im-
37 plies a scale-free dynamo, therefore indicating that a turbulent dynamo may act throughout
38 the convection zone. Moreover, from the slope of the emerging flux distribution the (tur-
39 bulent?) dynamo producing small-scale features produces considerably more flux than the
40 active-region dynamo at the tachocline.
41

42
43 **Keywords** Sun: magnetic field · Sun: photosphere
44

45
46 L.M. Thornton (✉) · C.E. Parnell
47 School of Mathematics and Statistics, University of St Andrews, North Haugh, St Andrews,
48 Fife KY16 9SS, UK
49 e-mail: lynsey@mcs.st-and.ac.uk
50

1. Introduction

Magnetic flux is omnipresent on the Sun over a wide range of size scales spanning many orders of magnitude in flux and area. Active regions involve large-scale magnetic features such as sunspots and plage regions and have fluxes of a few times 10^{22} Mx (Maxwell). The quiet Sun involves two types of features, network fields and intranetwork (IN) fields. Network features have fluxes of $\approx 10^{18} - 10^{19}$ Mx (Martin, 1988; Wang *et al.*, 1995) and their field extends out into the solar atmosphere, producing a ‘network’ of connections that (practically) interlink all magnetic features. The network itself is comprised of mixed polarity features which reside in supergranular lanes and vertices. These mixed polarity features are sustained by ephemeral regions, decaying active regions and the coalescence of IN fields (Schrijver *et al.*, 1997). The network field is very dynamic and evolves on supergranular time scales. Hence, the lifetime of network features is typically a few hours to a day.

Within supergranular cells there exist IN fields which have a typical size of $10^{16} - 10^{18}$ Mx (Livingston and Harvey, 1975; Zirin, 1985, 1987; Keller *et al.*, 1994; Wang *et al.*, 1995). The lower limit of these feature’s flux is a reflection of the current resolution of instruments. In photospheric magnetograms, IN fields are observed as mixed-polarity magnetic flux on a scale less than 1 Mm (Livingston and Harvey, 1975; Smithson, 1975; Livi, Wang, and Martin, 1985; Zirin, 1985, 1987; Martin, 1988; Wang, 1988; Wang *et al.*, 1995). Despite their small scale it is thought that IN fields contribute a significant fraction to the total solar magnetic flux (see *e.g.* Socas-Navarro and Sánchez Almeida, 2002). There is considerable interest in understanding the origin and behaviour of magnetic fields, including determining the size of the smallest magnetic features on the Sun (see *e.g.* Sánchez Almeida, Emonet, and Cattaneo, 2003; Socas-Navarro, Martínez Pillet, and Lites, 2004; Manso Sainz, Landi Degl’Innocenti, and Trujillo Beuno, 2004; Khomenko *et al.*, 2005; Domínguez Cerdeña, Sánchez Almeida, and Kneer, 2006; Rezaei, 2007; Sánchez Almeida, 2007; Harvey *et al.*, 2007; Orozco Suárez *et al.*, 2008; Lites *et al.*, 2008).

Flux features in the quiet Sun are highly dynamic and evolve constantly during their life on the solar surface. There are four key processes that may affect flux features: emergence, fragmentation, merging and cancellation (Schrijver *et al.*, 1997; Parnell, 2001). Emergence is the process by which flux, in the form of flux loops, is brought into the solar atmosphere from the convection zone. It is associated with the appearance of opposite-polarity flux features in the photosphere, which should have a net flux of zero. The new flux regions, assumed to be bipolar and known as ephemeral regions, increase in flux and grow in area as the flux loops emerge. Fragmentation involves the splitting of a single, large feature into two or more smaller features. The converse of this is merging, where two or more like-polarity features coalesce to form a single, larger feature. Cancellation of flux occurs when two opposite-polarity features come into close proximity leading to either flux decreasing through submergence below the photosphere or decreasing by lifting of a closed magnetic loop into the corona.

Harvey *et al.* (1999) found, using simultaneous magnetograms taken in the photosphere and chromosphere, that in the quiet Sun the former is the cause of 44% of cancellations, whilst the latter only accounts for 18% (for the remaining 38% they were unable to decipher the mechanism). Depending on the initial flux of each feature, cancellation causes partial or full removal of the flux features.

In this paper, we focus on small-scale flux emergence. Emergence of flux into the quiet Sun occurs through the emergence of ephemeral regions, which tend to appear close to supergranular boundaries (Wang, 1988; Schrijver *et al.*, 1997). Once emerged, flux from ephemeral regions quickly disperses into the surrounding network, giving lifetimes

101 for ephemeral regions of a few hours to a few days (see *e.g.* Harvey and Martin, 1973;
102 Title, 2000; Hagenaar, 2001). Ephemeral regions have flux in the range of $10^{18} - 5 \times 10^{19}$ Mx
103 (Harvey, 1993; Chae *et al.*, 2001; Hagenaar, 2001; Hagenaar, Schrijver, and Title, 2003),
104 with the lower limit on the flux attributed to instrumental limitations. A flux emergence rate
105 of ephemeral regions, over the whole solar surface, has been estimated at between $1.8 -$
106 110×10^{22} Mx day⁻¹ ($0.29 - 18.06$ Mx cm⁻² day⁻¹) (Harvey, Harvey, and Martin, 1975;
107 Harvey, 1993; Title, 2000; Chae *et al.*, 2001; Hagenaar, 2001; Hagenaar, Schrijver, and Title,
108 2003; Hagenaar, DeRosa, and Schrijver, 2008). The frequency of emergence of ephemeral
109 regions, over the solar surface, was found to be part of a smoothly decreasing distribution
110 that spanned four orders of magnitude in flux, between $10^{18} - 10^{22}$ Mx, eight orders of mag-
111 nitude in emergence frequency (Hagenaar, Schrijver, and Title, 2003). There are known to
112 be small-scale emergence events occurring with $\leq 10^{17}$ Mx in flux (Zirin, 1987), but it is
113 unclear if the above distribution continues down to lower fluxes. In this paper, we address
114 this question.

115 In order to quantify small-scale flux emergence, we use automatic identification methods
116 to determine the number and characteristics of ephemeral regions in a sequence of derived
117 magnetogram data from the Narrowband Filter Imager (NFI), which is part of the Solar
118 Optical Telescope (SOT) on board *Hinode*. This involves pre-processing of the data, dis-
119 crimination of features from background and finally identification of emerging flux. The
120 *Hinode*/NFI data sequence and its preparation and corrections are reviewed in Section 2. In
121 Section 3, we explain the methods used to identify and track flux features, whilst Section 4
122 considers three methods to detect emerging flux. The results of each method are given in
123 Section 5 and a comparison of the results is discussed in Section 6. The final conclusions
124 are presented in Section 6.

2. Data

125
126
127
128 A near disk centre data sequence was obtained on 19 September 2007 between 12:44 UT
129 and 17:43 UT from NFI, using the Na I D₁ resonance line at 5896 Å, in the Solar Optical
130 Telescope (SOT) package aboard *Hinode* (Kosugi *et al.*, 2007; Tsuneta *et al.*, 2008). Line-
131 of-sight high-resolution magnetograms were derived from the observed Stokes parameters
132 I and V by first subtracting the NFI pedestal of 800 digitiser counts from each V , I pair.
133 The *Hinode* data were calibrated by comparison with MDI data as SOT calibration was
134 unavailable at the time of preparation of the data. Later on in this paper, we compare our
135 results with those found using MDI and other instruments and the results compare well, and
136 therefore we feel that our calibration has been reasonable. We use the conversion factor of
137 Lamb *et al.* (2010), who also analysed this particular data set, and multiply the pixel ratios
138 V/I^* by 6555 Mx cm⁻², where $I^* = I - 2 \times 200 \times \text{FGNINT}$. FGNINT is taken from the
139 header information and, in this case, is eight. We only use the lower right hand section of
140 the original field of view, because of the reported glint near the left hand side of the NFI's
141 field of view (C. E. DeForest, private communication) and due to the presence of the *Hinode*
142 oil drop in the upper right hand portion of the image (Ichimoto *et al.*, 2008). The final field
143 of view is 853×600 pixels, which corresponds to 99×70 Mm (136×96 arcsec), as seen
144 in Figure 1a. The data were then deconvolved using an NFI point-spread function (C. E.
145 DeForest, private communication) and despiked using 'zspike' (DeForest, 1998). Images
146 were also smoothed temporally by applying a 3 min FWHM Gaussian weighting function
147 and smoothed spatially by applying a two pixel FWHM Gaussian kernel. The original image
148 cadence was approximately 45 s, but was reduced to a precise 90 s between each image
149 during the temporal smoothing. The resultant data set has 200 images that span 5 h.

150

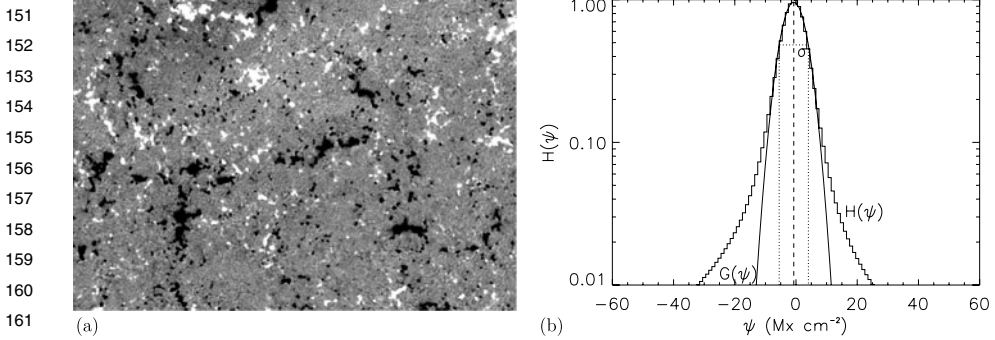


Figure 1 (a) Example magnetic field image taken on 19 September 2007 at 12:52:14 UT after processing and data correction, with pixel saturation at $\pm 30 \text{ Mx cm}^{-2}$. (b) Histogram, $H(\Psi)$, of the pixel fluxes. A Gaussian, $G(\Psi)$, is fitted to the core of the histogram (solid), with the centre of the Gaussian (dashed) and FWHM (dotted) marked.

An estimate of the residual noise of the data, after processing, is required for the identification of flux features and is measured by fitting a Gaussian curve to the core of the histogram of pixel values, as described in Hagenaar *et al.* (1999) (Figure 1(b)). We define the noise, σ , to be equal to the half-width half-maximum of the Gaussian. Here, $\sigma = 4.05 \text{ Mx cm}^{-2}$. By picking only pixels with values of $m\sigma$ or greater (where, here $m = 2$), we reduce the risk of identifying spurious features.

3. Feature Identification and Tracking

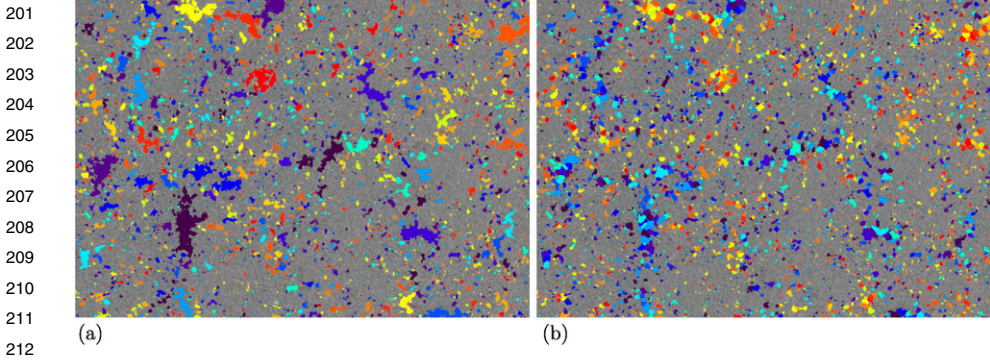
The aim of a feature identification algorithm is to set flux features apart from the background noise in an objective manner. However, definitions of flux features vary and so the results of the algorithms are sensitive to the methods used and the assumptions made (DeForest *et al.*, 2007; Parnell *et al.*, 2009). There are three main algorithms: clumping, downhill and curvature (DeForest *et al.*, 2007). We apply the first two, which are described below.

The clumping identification algorithm identifies features as groups of same-sign contiguous pixels that have absolute flux above a given lower cutoff, equal to 2σ (Parnell, 2002; Parnell *et al.*, 2009). These features are known as flux massifs. A minimum feature area of four pixels is applied to help eliminate the false identification of features, as discussed in DeForest *et al.* (2007). Figure 2(a) shows the example frame from Figure 1(a) with the flux massifs, found using the clumping identification method, coloured.

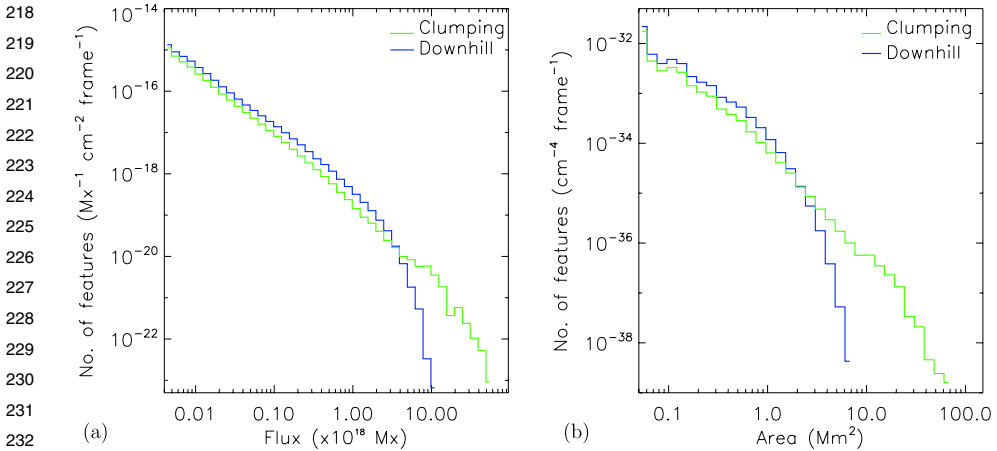
In the downhill identification algorithm, features are defined to be groups of contiguous same-sign pixels with flux above a lower cutoff (also equal to 2σ) that are singly peaked, *i.e.*, they are formed by dividing the features found using the clumping method, along saddle lines (Welsch and Longcope, 2003). This method is called ‘downhill’ because each feature only has a single maximum in absolute flux and all pixels decrease in absolute value (flow downhill) as you move away from the maximum. These features are known as flux peaks. As in clumping, features are excluded if they have an area of less than four pixels. Using the same example frame as that in Figure 1(a), we have coloured the flux peaks in Figure 2(b). Clearly, the flux massifs in Figure 2(a) are typically larger than those in Figure 2(b), as one expects.

By comparing the two frames in Figure 2, it is clear that there are differences between the features identified by the clumping and downhill methods, as detailed in Table 1 and

Small-Scale Flux Emergence Observed Using *Hinode*/SOT



213 **Figure 2** (a) Flux massifs identified using the clumping method and (b) flux peaks identified using the
 214 downhill method identified in the same NFI example frame as in Figure 1(a). The blues and purples are the
 215 negative features, whilst the reds and yellows are the positive features. The background pixels have been
 216 saturated at $\pm 30 \text{ Mx cm}^{-2}$.



233 **Figure 3** Histograms showing the probability distributions of (a) fluxes and (b) areas of the features identified
 234 by the clumping and downhill algorithms.

237 Figure 3. From Table 1 (top), we can see that the downhill method identifies approximately
 238 1.5 times as many features as the clumping method, but the mean flux of each downhill
 239 feature is approximately 1.5 times less than the mean flux of the clumping features and
 240 similarly for feature areas. Hence, downhill and clumping observe more-or-less the same
 241 total flux from all features, as one would expect. In Figure 3, histograms of the feature
 242 fluxes and areas show that at the small end of the distribution scale (less than $3 \times 10^{18} \text{ Mx}$
 243 in flux and 2 Mm^2 in area) the downhill method identifies more features than the clumping
 244 method. At larger scales, the downhill distribution drops off rapidly with only clumping
 245 identifying features with fluxes above 10^{19} Mx and areas above 6 Mm^2 .

246 Two of the methods applied to detect emergence, which are described in the following
 247 section, require that the flux features are tracked in time throughout the data. This enables
 248 the evolution of the features to be followed and the peak flux, peak area and lifetime of each
 249 tracked feature to be found. A brief description of feature tracking is given here, but the full
 250

251 details are discussed in Appendix A. Tracking involves associating like-polarity features
 252 in consecutive frames. Once tracking is complete, each feature has a unique label, which
 253 remains with it for its entire life. This means that the frame and nature of birth of all fea-
 254 tures can easily be determined. The birth of a feature can be classed as either ‘appeared’
 255 (through emergence or coalescence of sub-resolution flux) or ‘appeared through fragmen-
 256 tation’ (when a feature breaks off from another feature). Further filtering is applied to the
 257 tracked data with tracked features lasting less than four frames being removed. The results
 258 of the feature tracking are presented in Table 1 (bottom).

259 The tracked feature characteristics presented in Table 1 (bottom) reveal that there are
 260 approximately 93% less tracked massifs and tracked peaks than there are individual flux
 261 massifs or flux peaks. This is due to the fact that the tracked massifs and tracked peaks have
 262 mean lifetimes of about 14 and 9 min (nine and six frames), respectively, in comparison to
 263 the individual flux massifs and peaks, which last just one frame by definition. The mean
 264 lifetime of the tracked peaks identified by the downhill method, is about 3/5 of the lifetimes
 265 of tracked massifs identified by the clumping method. This is because flux peaks are more
 266 susceptible to local fluctuations in the data due to either granulation or noise, as discussed by
 267 Parnell *et al.* (2009). By filtering out the shortest-lived features we reduce the total overall
 268 flux that is counted by just 5% and 6%, respectively, for flux massifs and flux peaks.

270 Now that the features can be followed over their lifetimes, we can calculate the mean
 271 peak flux of the tracked features. Interestingly, these peak fluxes are lower, by 24% and 25%
 272 respectively, than the mean flux of the individual flux massifs (clumping) or peaks (down-
 273 hill). This counter intuitive result arises because we find that large features are typically long
 274 lived (see *e.g.*, Lin and Rimmele, 1999) and, for the mean peak flux, we simply count a sin-
 275 gle (the maximum) flux value for each tracked feature rather than the flux of the feature in
 276 every frame. Hence, the number of large fluxes is considerably reduced when calculating the
 277 mean peak flux of the tracked features, thus lowering the mean. However, we find that the
 278 mean peak areas of the tracked features are very similar to those of the individual features
 279 indicating that the filtering out of the shortest-lived features does not remove a significant
 280 fraction of the smaller features.

281
282
283 **Table 1** Characteristics of the
 284 identified and tracked features
 285 from both the clumping and
 286 downhill feature identification
 287 methods.

Identified features	Clumping	Downhill
Number of features identified ($\times 10^{-16}$ cm $^{-2}$ day $^{-1}$)	369.2	542.8
Mean feature flux ($\times 10^{17}$ Mx)	1.7	1.2
Mean feature area (Mm 2)	0.5	0.3
Total absolute flux (Mx cm $^{-2}$ frame $^{-1}$)	6.6	6.7
Tracked features	Clumping	Downhill
Number of tracked flux features ($\times 10^{-20}$ cm $^{-2}$ day $^{-1}$)	24.3	37.9
Mean tracked feature peak flux ($\times 10^{17}$ Mx)	1.3	0.9
Mean tracked feature peak area (Mm 2)	0.5	0.4
Mean tracked feature lifetime (min)	15	9
Total absolute flux (Mx cm $^{-2}$ frame $^{-1}$)	6.3	6.3

4. Detection of Flux Emergence

The main aim of this paper is to estimate the frequency of emergence of small-scale flux. In order to do this, we compare the results from three approaches for finding emerging flux regions. Emergence is the process by which new flux is introduced into the solar atmosphere from the convection zone below, but it is not the only process by which new flux features can ‘appear’ in magnetograms. There are, in fact, three processes of ‘appearance’ (Lamb *et al.*, 2008). In addition to emergence, new features can appear following fragmentation or when sub-resolution flux merges together to form a feature, which can then be identified using a feature identification algorithm. Since, we are interested in the rates of genuine flux emergence any method must be able to distinguish between the above types of appearance.

We apply three methods of flux emergence detection to the clumping and downhill data sets. Two of our methods assume flux emerges in the form of bipolar pairs of opposite-polarity flux features (Bipole Comparison and Tracked Bipolar), as illustrated by the cartoon in Figure 4 (top). The third method assumes that flux emerges in the form of opposite-polarity clusters of features (Tracked Cluster), as the cartoon in Figure 4 (bottom) shows. In such an emergence, the sum of the fluxes of all the emerging positive features should equal the sum of the fluxes of all the emerging negative features. Zwaan (1985) described the emergence of active regions as a process that occurs along these lines and Wang *et al.* (1995) observed this as the process of small-scale IN emergence.

The other key difference between the methods is whether they are applied to the individual features or to the tracked features, as suggested by the names of the methods and explained below. The three methods are briefly described below, with full details given in Appendices B, C and D.

• Bipole Comparison Method

The bipole comparison method (BC) method is based on our interpretation of the emergence detection method used by Hagenaar (2001), which itself was based on a detection approach by Harvey (1993). It assumes bipolar emergence and is applied to the identified features which have not been tracked. This method uses three steps to detect emerging bipoles:

- *Bipole Identification*: In frame j , the i th positive feature Φ_{i+}^j , with flux Ψ_{i+}^j , and the i th negative feature Φ_{i-}^j , with flux Ψ_{i-}^j , are deemed to be a bipole if the shortest distance between their boundaries is ≤ 7 pixels ≈ 0.8 Mm and

$$\frac{1}{3} \leq \frac{|\Psi_{i+}|}{|\Psi_{i-}|} \leq 3.$$

- *Detecting Emerging Bipoles*: To detect the bipoles that are emerging in frame j , we compare the features of the bipoles in frame j with those in the frame $j - 1$ to see if they are newly appeared in frame j . If any of the bipole’s features are not newly appeared we determine whether these feature’s fluxes have increased or decreased between frames $j - 1$ and j . To be an emerging bipole both features of the bipole must be either newly appeared or one feature must be newly appeared and the other increasing in flux.
- *Selecting Unique Pairings*: At this stage, it was found that many of the emerging bipoles did not constitute unique feature pairings. This occurred if: *i*) a true bipole coincidentally emerged close to other appearances or *ii*) a cluster of positive and a cluster of negative features emerge together. We divided the non-unique feature pairings into one of these categories by finding, in each frame, which features have like-polarity emerging neighbours. The pairings involving features with neighbours are likely to be part of

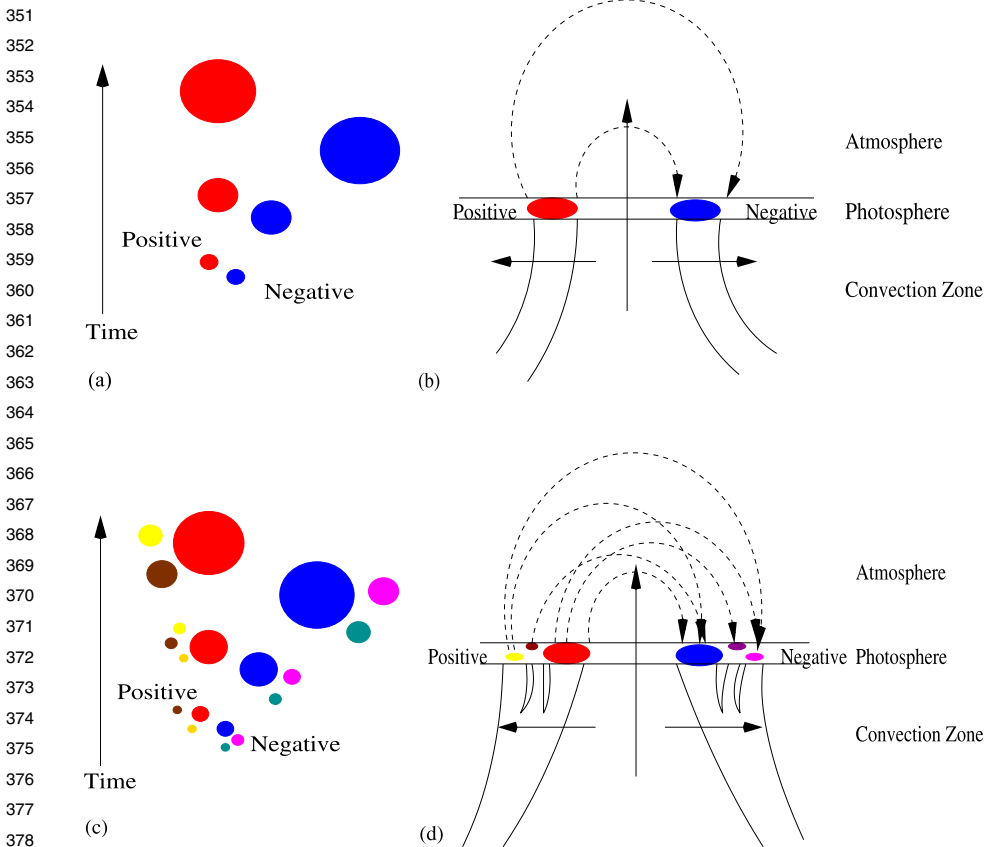


Figure 4 A cartoon of (top) bipolar and (bottom) cluster emergence as seen in (left) the photosphere and (right) a vertical cut.

cluster emergences and so were retained. For the remaining non-unique pairings, the flux ratios of the features in each bipole are compared and the bipole with the ratio closest to unity is regarded as the true emerging bipole and is retained. The others are removed.

For full details on this method see Appendix B.

• Tracked Bipolar Method

The data used by Hagenaar (2001) had a 96 min cadence and so there were few cases where the same flux emergence events were observed in multiple frames. Here, however, our data are just 90 s apart and we find that emerging flux events are frequently observed in successive frames. Using the BC method could mean that these emergence events are counted multiple times as they emerge. To avoid this problem a second flux detection method, the tracked bipolar method (TB), is applied to the tracked data. It still assumes that emergence events are bipolar and, like the BC method, there are three steps to find emerging bipoles.

– *Bipole Identification*: Same procedure as in the BC method.

– *Identifying Emerging Bipoles*: Using the birth information obtained after feature tracking we classify a bipole as an emerging bipole if the bipole's features are both flagged

401 as ‘appeared’ or one is flagged as ‘appeared’ and the other is flagged as ‘appeared’
402 through fragmentation’. Furthermore, the two features of the bipole must have been
403 born within ten frames (15 min) of each other.

404 – *Selecting Unique Pairings*: Same procedure as in the BC method.

405 For full details on this method see Appendix C.

406 • **Tracked Cluster Method**

407 Visual inspection of the data appears to show quite a number of emergence events involv-
408 ing clusters of opposite-polarity features. Consequently a third method aimed at address-
409 ing this issue was developed. The tracked cluster method (TC) is applied to the tracked
410 data, but this time assumes cluster-like emergence instead of bipolar emergence. The three
411 steps of this method differ from those used in the two previous methods.

412 – *Identifying Feature Emergence*: The birth information obtained from tracking the fea-
413 tures is used to identify the first ten frames of a feature’s life (if a feature lasts for less
414 than ten frames, then every occurrence of the feature is considered). If the flux and area
415 of the feature are initially small, $\leq 2.7 \times 10^{17}$ Mx and ≤ 0.3 Mm² respectively, then the
416 feature is classed as ‘recently appeared’.

417 – *Finding Like-Polarity Clusters*: An ‘association’ matrix is created that identifies which
418 like-polarity recently-appeared features are a short distance from one another. A group
419 of such features is defined as a cluster. If the features in this cluster all appear within
420 ten frames (15 min) of each other then the cluster is classified as ‘recently appeared’.
421 Note that not all of the features identified in the first step end up being associated with
422 other such like-polarity features.

423 – *Finding Opposite-Polarity Connections*: By dilating all ‘recently appeared’ lone fea-
424 tures, or all features of a ‘recently appeared’ cluster by four pixels (465 km) in frame
425 j , we compare these pixels to the same pixels in frames $j - 2$, $j - 1$, $j + 1$ and $j + 2$.
426 If a recently-appeared lone feature or cluster overlaps another recently-appeared lone
427 feature or cluster with the opposite-polarity then these recently-appeared features are
428 grouped to form an emerging event, which will either be bipolar or cluster-like in na-
429 ture.

430 For full details on this method see Appendix D.

431

432

433

433 **5. Flux Emergence Results**

434

435

435 5.1. Emerging Event Characteristics

436

437

438

439

440

441

442

443

444

445

446

447

448

449

450

The results from all three emergence event detection methods applied to both the clumping and downhill data are given in Table 2. It can be seen that fewer emerging events are identified in the clumping data than in the downhill data for each method, which is consistent with the feature identification and tracking results from Section 3. However, a comparison of the number of emerging events detected by each method shows that the BC method detects many more emerging events than the two tracked methods. This is because our data have a 90 s cadence and thus the BC method multiply counts events that last longer than 90 s, as we anticipated would be a problem. Note, however, that multiple counting of events is not the only problem with the BC method. If we multiply the number of tracked emerging events found by the TB and TC methods by the mean number of frames these emerging events live (a mean of ≈ 7 frames and ≈ 12 frames, respectively) then we find 55–61% and 37–48% fewer events than found using the BC method applied to the clumping and downhill data, respectively. This means that the BC method seems to not only be multiply counting the

Table 2 Results from the three emergence detection methods (BC – Bipole Comparison, TB – Tracked Bipolar and TC – Tracked Cluster) applied to both data sets (c – clumping and d – downhill).

Emergence event characteristics	Emergence detection method					
	BC		TB		TC	
	c	d	c	d	c	d
No. of emerging events identified ($\times 10^{-16} \text{ cm}^{-2} \text{ day}^{-1}$)	61.5	79.0	4.2	7.1	2.3	2.6
No. of flux features involved in emergence ($\times 10^{-16} \text{ cm}^{-2} \text{ day}^{-1}$)	94.9	116.6	7.4	11.1	8.5	10.6
Mean peak emerging event flux ($\times 10^{16} \text{ Mx}$)	8.8	5.4	11.0	7.1	14.0	14.1
Mean peak emerging event area (Mm^2)	0.4	0.3	0.7	0.5	1.0	1.0
Percentage of retained non-unique pairings	66	73	45	55	55	60
Mean tracked emerging event life (min)	n/a	n/a	10.7	11.0	18.8	18.2
Total absolute emerged flux ($\text{Mx cm}^{-2} \text{ day}^{-1}$)	470.4	341.4	38.9	50.2	32.6	38.8

emerging events found by these two tracked methods, but it is also identifying extra bipoles as emerging events. Considering the reduction of the number of tracked features compared to identified features due to lifetime filtering, it is likely some of these extra events involve features that live for less than four frames, but, as will be discussed later, these are not the only extra events counted by the BC method.

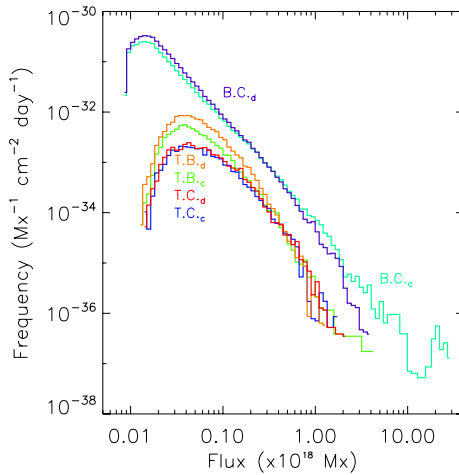
It is clear that there is a dramatic difference in the number of emerging events between the BC method and the tracked methods, but what about the characteristics of the emerging events. Not surprisingly, the peak fluxes and areas of the emerging events found by the TB and TC methods are larger than those found by the BC method since the features are tracked. The peak fluxes and areas of the TC events are also larger than those found by the TB method, since most of TC events involve more than two features. Accordingly the upper bound on the total absolute emerging flux detected per frame is given by the BC method and the lower bound is given by the TB method.

The differences in the number of emerging events and the mean emerging event fluxes, between the methods, can be seen in Figure 5. Figure 5 is a log-log plot showing the probability distribution of fluxes from emergence events found by each emergence detection method, in both the clumping and downhill data sets. As expected, the distributions found by the BC method using the clumping and downhill data are higher than those found for the TB or TC methods, since the events are counted multiple times. For the BC method the distribution found using the clumping data extends to larger fluxes than that found using the downhill method, in line with what is already known about the distributions of flux massifs and flux peaks (Parnell *et al.*, 2008). All four of the distributions found by the tracked methods are similar, with the methods applied to the downhill data finding marginally more events with higher peak fluxes than the methods applied to the clumping data. It is clear that the BC method finds not only many more small-scale bipoles, but also, in the clumping data set, many more large-scale bipoles too, than the two tracked methods. This suggests that the extra emerging events found using the BC method involve not only features with very small flux, but also features with unusually large flux.

From Figure 5 we also note that the distributions of emerging event fluxes appear to follow a power law. As the distributions are only over a few orders of magnitude we cannot determine the slopes at the moment with any great certainty, however in Section 5.3 we

Small-Scale Flux Emergence Observed Using *Hinode*/SOT

501 **Figure 5** Log – log plot of
502 frequency of emergence against
503 emergence event fluxes. The
504 results from all three emergence
505 detection methods (BC, TB, and
506 TC) applied to both the clumping
507 (subscript ‘c’) and the downhill
508 (subscript ‘d’) data are plotted.



509 compare our results to previous results to determine if there is a single power law distribution
510 extending over all emerging features.

511 From Table 2 it can be seen that all three emergence detection methods detect high numbers of
512 non-unique bipole pairings. The TC method was designed specifically to identify cluster
513 emergence events, to better gauge how numerous they are. The numbers of clusters
514 that are identified using the TC method, as opposed to bipoles is $1.28 \times 10^{-16} \text{ cm}^{-2} \text{ day}^{-1}$
515 and $1.57 \times 10^{-16} \text{ cm}^{-2} \text{ day}^{-1}$ for the clumping and downhill data, respectively. In comparison
516 the TB method finds the number of non-unique events in the clumping and downhill data
517 to be $1.8 \times 10^{-16} \text{ cm}^{-2} \text{ day}^{-1}$ and $3.8 \times 10^{-16} \text{ cm}^{-2} \text{ day}^{-1}$. It is found that the non-unique
518 pairings typically consist of one positive feature associated with two negative features or vice
519 versa, so that the number of clusters in the TB method would be $0.9 \times 10^{-16} \text{ cm}^{-2} \text{ day}^{-1}$
520 in the clumping data and $1.9 \times 10^{-16} \text{ cm}^{-2} \text{ day}^{-1}$ in the downhill data.

521 The following section presents a visual comparison of the three emergence detection
522 methods, which will help to further our understanding of the differences and similarities
523 between each of the methods.

5.2. Visual Comparison of Emergence Events Found by the Three Detection Methods

524 A comparison of the individual emergence events detected by each method reveals that 1/3
525 of events found in the clumping and downhill data are identified by all three methods. This
526 fraction is increased to 3/5 of events identified in both the clumping and downhill data when
527 just the TB and TC methods are compared and 3/4 when comparing either of the tracked
528 methods to the BC method.

529 Figure 6 shows an example of an emerging event which is identified identically by all
530 three methods. It was found that emerging events are more likely to be identified by all three
531 methods if they occur in a relatively flux free region. However, emergence often occurs
532 in regions which contain many other features. In these cases, the newly emerged pair or
533 clusters of opposite-polarity features often become connected to pre-existing surrounding
534 features very quickly and so rapidly lose their own bipolar or cluster identity and thus they
535 become hard to identify.

536 As the results in Section 5.1 show, the BC method identifies many more emerging fea-
537 tures than the two tracked methods. Visual inspection of the results reveals that in the BC

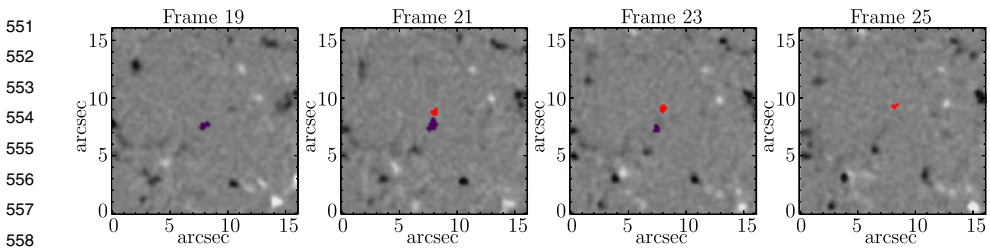


Figure 6 Example of a bipole (positive feature – red and negative feature – purple) identified by all methods.

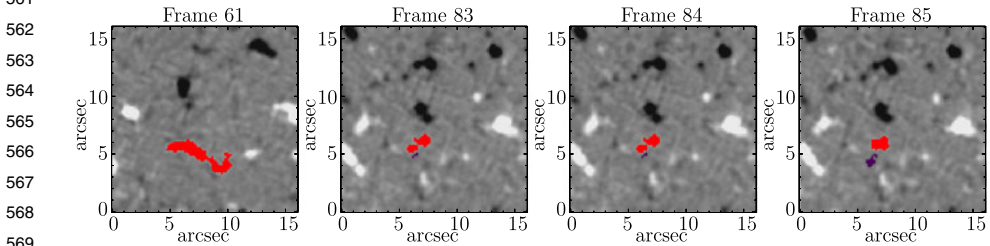


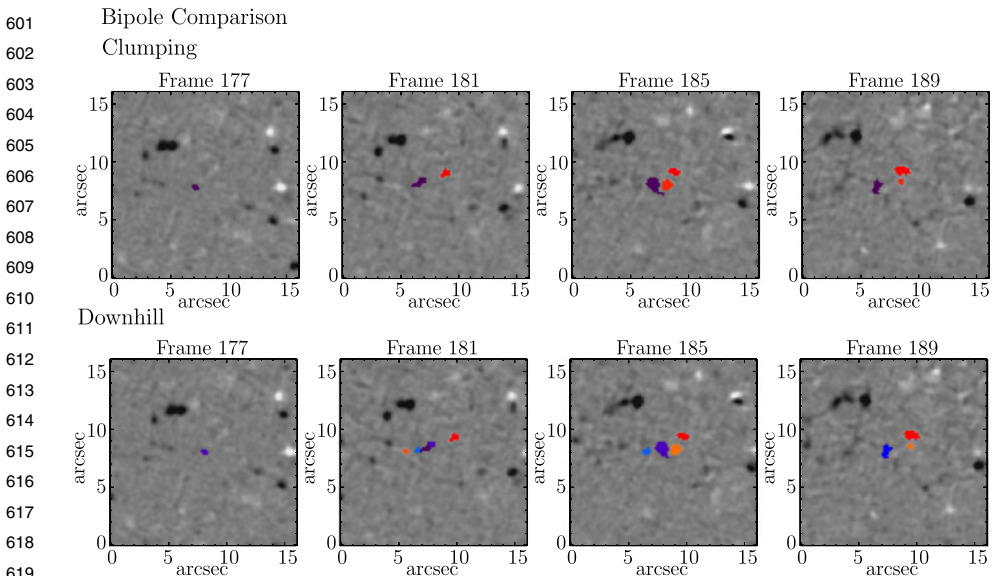
Figure 7 Example of where the Bipole Comparison method associates a long-lived (positive – red) feature, which was born in frame one (we only show it from frame 61), with a newly appeared (negative – purple) feature, born in frame 63, to create a false bipole emergence.

method many long-lived features whose flux is increasing (by, for example, coalescence of sub-resolution flux) are often paired with newly ‘appeared’ features created by an accumulation of sub-resolution flux that raises them above the detection threshold so they can be identified.

An example of this type of behaviour is shown in Figure 7, where a long lived positive (red) feature, which has been in existence since frame one, becomes paired with a newly appeared negative (purple) feature in frame 84. To identify this so-called emergence, the BC method only considers frames 83 and 84, which alone appear to give reasonable evidence of emergence. It is only apparent after the data have been tracked that this is not really an emergence and that the positive feature has already been in existence for quite sometime. In a system as dynamic as the small-scale quiet Sun this can often occur. These types of events are not identified by either of the tracked methods since in these methods all the features of an emergence event must be born within ten frames (15 min) of each other. This again suggests that the BC method produces an over-estimate of the rate of flux emergence in the quiet Sun.

The structure of emerging events identified by the three methods also varies. We find that more cluster-type emergence is found in the downhill data than in the clumping data for each method, which is not surprising, since a single feature in the clumping data is often identified as two or more features in the downhill data (Parnell *et al.*, 2009). On analysing cluster emergence from all three detection methods, the majority were found to involve a feature of one polarity associated with two of the opposite polarity. However, following the evolution of cluster emergences reveals that most eventually evolve into bipoles, once the features are fully emerged. Furthermore, in complex cases of cluster emergence, the three methods often identify different features as being involved. Due to the more stringent constraints of the TB method, it tends to try and simplify all emerging events into bipoles no matter how complex they are. On the other hand, the BC and TC methods may connect

Small-Scale Flux Emergence Observed Using *Hinode*/SOT



620 **Figure 8** A cluster emergence identified by the BC method (negative features – purples and blues and
621 positive features – reds and oranges) in the clumping data (top row) and downhill data (bottom row). Clearly,
622 in the downhill data more and slightly different features are detected than in the clumping data.

623
624 unlikely features to the emerging clusters. Figures 8, 9, and 10 illustrate this by showing
625 how the same complex emergence event is identified by the three methods.

626 Overall, none of the flux detection methods is perfect, as is apparent on visual inspection
627 of the data. There are probably still emergence events that all three methods miss, although
628 these cases are rare, and also each method identifies some events that are questionable.

630 5.3. Rates of Flux Emergence

631
632 Parnell *et al.* (2009) found that the distribution of all photospheric feature fluxes, from small-
633 scale intranetwork features right up to sunspots, follows a single power law. Furthermore,
634 Hagenaar, Schrijver, and Title (2003) suggested that the fluxes of newly emerged features
635 follow a power law. From Figure 5, we find that the distributions of the fluxes of our emer-
636 gence events also appear to follow power laws which fall off at small-flux events due to
637 resolution limitations and our strict tracking criteria. The key question, of course, is whether
638 or not we find a single power law for all fluxes of emerging events, which would allow us to
639 find a global flux emergence rate.

640 Hagenaar, Schrijver, and Title (2003) used quiet-Sun MDI high resolution data to deter-
641 mine the distribution of ephemeral regions with fluxes between 5×10^{18} and 10^{20} Mx. They
642 compared their quiet-Sun ephemeral region results with emergence results from Harvey and
643 Zwaan (1993) for active region. However on their Figure 11 the numbers of these bipoles is
644 a factor hundred higher than it should be (C.J. Schrijver, private communication). Hagenaar,
645 Schrijver, and Title (2003) concluded that bipolar emergence follows a smoothly decreasing
646 distribution over nearly four orders of magnitude in flux and eight orders of magnitude in
647 frequency with a power-law index of ≈ -2.2 . If the active region data are plotted correctly
648 then an even better agreement between these two data sets is found and they follow a steeper
649 power-law distribution with an index of -2.88 . In Figure 11, we compare our results with
650

651

652 Tracked Bipole
653 Clumping

654

655

656

657

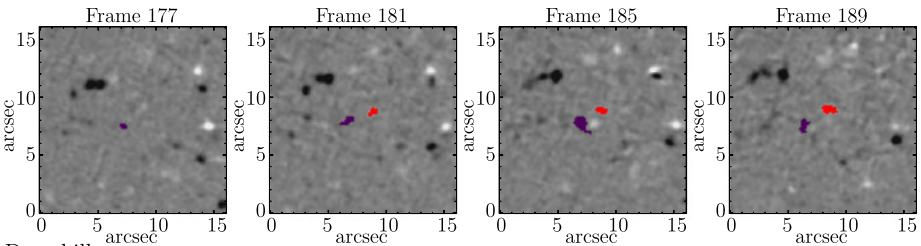
658

659

660

661

662



662 Downhill

663

664

665

666

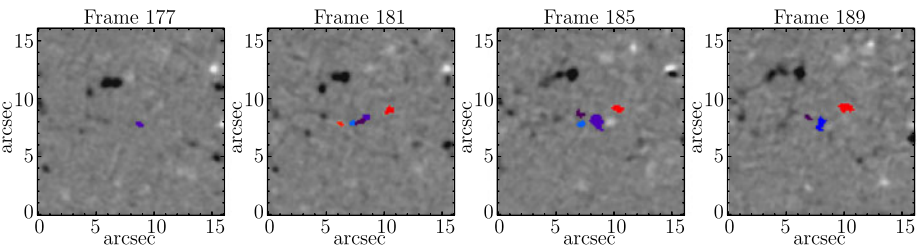
667

668

669

670

671



672

672 **Figure 9** As Figure 8, but this time the cluster emergence is detected using the TB method. Due to its strict
673 criteria of emergence, the TB method rarely detects cluster emergence events and instead only finds bipolar
674 emergences.

675

676

677

677 Tracked Cluster
678 Clumping

679

680

681

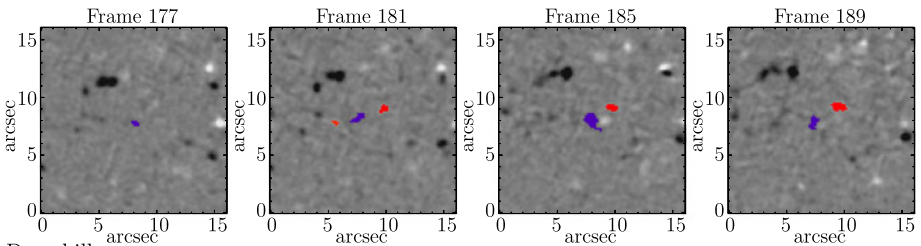
682

683

684

685

686



687 Downhill

688

689

690

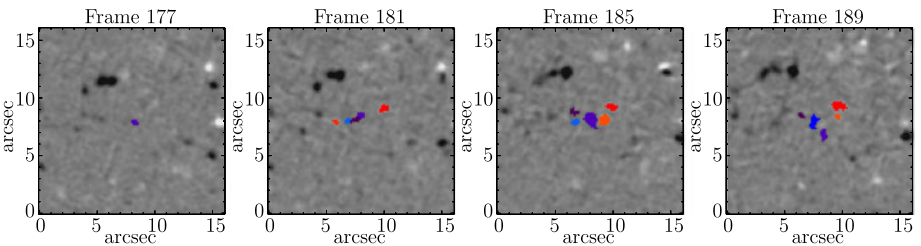
691

692

693

694

695



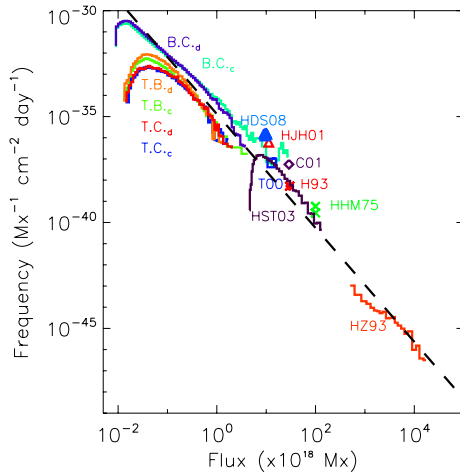
696 **Figure 10** As Figure 8, but this time the cluster emergence is detected using the TC method. Here, the TC
697 method has identified less(more) features involved in the emergence event in the clumping (downhill) data
698 than the BC method.

699

700

Small-Scale Flux Emergence Observed Using *Hinode*/SOT

701 **Figure 11** Log-log plot of the
 702 frequency of emergence against
 703 the emergence event fluxes. The
 704 power law fit, $N_{\text{all}}(\Phi)$ against Φ
 705 (dot-dashed line), has an index of
 706 $\alpha = 2.69$. Along with the
 707 distributions from this paper,
 708 results from the following papers
 709 are plotted: HHM75 (Harvey,
 710 Harvey, and Martin, 1975), H93
 711 (Harvey, 1993), HZ93 (Harvey
 712 and Zwaan, 1993), T00 (Title,
 713 2000), C01 (Chae *et al.*, 2001),
 714 HJH01 (Hagenaar, 2001), HST03
 715 (Hagenaar, Schrijver, and Title,
 716 2003), HDS08 (Hagenaar,
 717 DeRosa, and Schrijver, 2008).



718 **Table 3** Frequency of emergence and mean flux per emergence for ephemeral regions and active regions
 719 from various authors: HHM75 (Harvey, Harvey, and Martin, 1975), H93 (Harvey, 1993), HZ93 (Harvey
 720 and Zwaan, 1993), T00 (Title, 2000), C01 (Chae *et al.*, 2001), HJH01 (Hagenaar, 2001), HST03 (Hagenaar,
 721 Schrijver, and Title, 2003), HDS08 (Hagenaar, DeRosa, and Schrijver, 2008). *These results were not directly
 722 given in the paper, but have been determined from the presented results. †The active region results.

Paper	Instrument	Cadence	Mean emerging event flux ($\times 10^{18}$ Mx)	Frequency of emergence ($\times 10^{-21}$ cm $^{-2}$ day $^{-1}$)
HHM75	KP/NSO fd	2–6 h	100	2.95–6.08*
H93	KP/NSO fd	24 h	30	14.3*
T00	MDI hr	1 min	13	88.7*
C01	BBSO hr	2.5 min	28.9	169.5*
HJH01	MDI fd	96 min	11.3	722.8*
HST03	MDI fd	96 min	10.3*	198.3–390
HDS08	MDI fd	5 min	9.6*	1200–1610
†HZ93	KP/NSO fd	24 h	13413*	0.16–1640* $\times 10^{-5}$

735 not only theirs, but also results from other papers (listed in Table 3). Here, we see that the
 736 emerged fluxes follow the same distribution over nearly seven orders of magnitude in flux
 737 and nearly 18 orders of magnitude in frequency. A fit to the data reveals that the distribution
 738 of emerging event fluxes (dot-dashed line in Figure 11) is given by
 739

$$741 \frac{dN_{\text{all}}(\Phi)}{d\Phi} = \frac{n_0}{\Phi_0} \left(\frac{\Phi}{\Phi_0} \right)^{-\alpha}, \quad (1)$$

742 where $\Phi_0 = 10^{16}$ Mx, $-\alpha = -2.69$ is the power law index and $n_0 = 3.14 \times 10^{-14}$ cm $^{-2}$ day $^{-1}$
 743 is the total density of emerging events.

744 This power-law fit was computed using the following data sets: Hagenaar, Schrijver, and
 745 Title (2003), Harvey and Zwaan (1993), the downhill Bipole Comparison results and the
 746 downhill Tracked Bipolar results (above 4×10^{16} Mx). We only include these sets of results
 747 as they are all distributions over a (large) range of fluxes. The other results involve just single
 748

751 points at particular (average) fluxes representing the emergence frequency of all emerging
752 events with fluxes covering a (relatively) wide range. Naturally, these points tend to over-
753 estimate the true emergence rate at the given average flux. Also, we only include two of
754 our sets of results in order to provide a balance of the results at the small-scale end of the
755 distribution. The fitted power-law has a slope that is basically the same (within the error
756 bars) as the -2.88 slope found using the Hagenaar, Schrijver, and Title (2003) and Harvey
757 and Zwaan (1993) results alone.

758 Some authors consider the number of events per unit area per unit time which may be
759 determined by integrating Equation (1) with respect to Φ , to give

760
761
$$N_{\text{all}}(\Phi) = \frac{n_0}{(2 - \alpha)} \left(\frac{\Phi}{\Phi_0} \right)^{1 - \alpha}. \quad (2)$$

762

763 Clearly, the number of events per unit area per day also follows a power law with a slope
764 of -1.69 .

765 The flux emergence rate, F_{emer} , of emerging events over the range Φ_1 Mx and Φ_2 Mx is
766 then given by

767
768
$$F_{\text{emer}}(\Phi_1, \Phi_2) = \int_{\Phi_1}^{\Phi_2} \frac{dN_{\text{all}}(\Phi)}{d\Phi} \Phi d\Phi = \frac{n_0 \Phi_0}{2 - \alpha} \left[(\Phi/\Phi_0)^{2 - \alpha} \right]_{\Phi_1}^{\Phi_2}. \quad (3)$$

769
770

771 This allows us to determine the typical global rate of flux emergence into the photo-
772 sphere per day from events with fluxes between $\Phi_1 (\geq \Phi_0)$ Mx and Φ_2 Mx. For instance,
773 if we evaluate Equation (3) for $\Phi_1 = 10^{16}$ Mx and $\Phi_2 = 2 \times 10^{22}$ Mx, then a total of
774 ≈ 450 Mx $\text{cm}^{-2} \text{day}^{-1}$ is found to emerge. This would suggest that, at solar maximum, a
775 total of approximately $\approx 3 \times 10^{25}$ Mx is emerged per day into the solar atmosphere from
776 events with 10^{16} Mx or more.

777 Since the power law index of the flux probability distribution is less than -2 this implies
778 that the large-scale flux does not contribute significantly to the total photospheric flux on the
779 Sun. Indeed, the flux emergence rate of small-scale features with fluxes in the range 10^{16} –
780 10^{20} Mx is also ≈ 450 Mx $\text{cm}^{-2} \text{day}^{-1}$ and the emergence events with fluxes greater than
781 10^{20} Mx (*i.e.*, active regions) produce < 1 Mx $\text{cm}^{-2} \text{day}^{-1}$. So at solar minimum the same
782 $\approx 3 \times 10^{25}$ Mx is likely to emerge per day! This result suggests that it is the organisation of
783 the photospheric flux into large (active regions) or small (IN) features that determines the
784 structure of the solar atmosphere, not the global rate of flux emergence.

785 Note that we use 10^{20} Mx as the maximum for small-scale flux for two reasons. Firstly,
786 Hagenaar, Schrijver, and Title (2003) defined ephemeral regions as bipoles with a total ab-
787 solute flux below 3×10^{20} Mx. Secondly, Parnell *et al.* (2009) found, from the comparison of
788 flux distributions at solar minimum and solar maximum, that it was fluxes above this value
789 which tailed off during solar minimum.

790 Rates of flux emergence have been quoted for small-scale emerging events with fluxes of
791 various sizes lying in the range of 10^{16} – 10^{20} Mx (Harvey, Harvey, and Martin, 1975; Har-
792 vey, 1993; Title, 2000, Wang *et al.*, 1995; Hagenaar, 2001, 2008; Hagenaar, Schrijver, and
793 Title, 2003; Martínez González and Bellot Rubio, 2009). The rates quoted lie in the range of
794 1.8 – 110×10^{22} Mx day^{-1} over the whole surface (0.29 – 18.06 Mx $\text{cm}^{-2} \text{day}^{-1}$). However,
795 it is not easy to do a direct comparison between these results and our results as in many cases
796 a mean bipole flux is quoted, as opposed to the complete range for which the estimates are
797 made. However, our estimates are much larger than any previously quoted. The most likely
798 reasons for our larger emergence rates is the use of automated techniques for detecting the
799 emerging events. Our ability to track features in time and, hence, to count the maximum flux
800

801 of the emergence will naturally lead to a greater emergence rate. Furthermore, the range of
802 emerging event fluxes we consider are much wider than those quoted by others, since we
803 determine a global flux emergence rate for all events with flux greater than 10^{16} Mx. This
804 too will naturally produce a larger flux emergence rate.

805
806

807

808 6. Discussion and Conclusions

809

810 The aim of this paper is to determine the rate of flux emergence of small-scale (intranetwork)
811 ephemeral regions in the quiet-Sun photosphere. A 5 h sequence of quiet-Sun *Hinode*/NFI
812 data with a cadence of 90 s was examined in order to determine the emergence rate.

813 We first employed two different feature identification methods, clumping and downhill,
814 which identified features as flux massifs and flux peaks, respectively. Features were then
815 associated (tracked) between frames in order to determine their evolution. Three different
816 emergence detection methods were applied to the clumping and downhill data. The BC
817 emergence detection method was applied to the individual (untracked features). This method
818 assumes that the emergence of flux occurs through the emergence of bipolar pairs. The other
819 two emergence detection methods use the tracked features to search for emergence, with the
820 TB method assuming emergence involves bipolar pairs of features, whilst the TC method
821 seeks bipolar clusters of features.

822 Numerous emerging events are found with peak fluxes between 2×10^{16} Mx and
823 5×10^{19} Mx. The mean flux of the emergence events observed depends on the methods
824 used to identify the features and detect the emergence events and lies between 5×10^{16} –
825 14×10^{16} Mx. The mean area of the emergence events varies for similar reasons and lies in
826 the range $0.3 - 1.0$ Mm². These emergence events are therefore smaller than the ephemeral
827 regions detected by Hagenaar (2001) and Hagenaar, Schrijver, and Title (2003). Thus, they
828 may be thought of as intranetwork ephemeral regions. The number of emerging events de-
829 tected in our region of quiet Sun is between 2.3×10^{-16} to 7.1×10^{-16} cm⁻² day⁻¹, which
830 is equivalent to around 14 million to 43 million emergence events occurring per day with
831 mean fluxes between 2×10^{16} Mx and 5×10^{19} Mx. This may seem to be a significant num-
832 ber, but bearing in mind that many of the events are short lived, with mean lifetimes of just
833 10 – 19 min, at any one instant far fewer would be visible on the solar surface.

834 By comparing the results from all three methods, statistically and visually, it is clear that
835 the BC method over-estimates the emergence rate through multiply counting events and by
836 mistakenly pairing long-lived features. On the other-hand the TB and TC approaches may
837 under-estimate the rates of emergence, since their strict criteria mean that emergence events
838 can sometimes be missed. We therefore use these results to provide bounds for the true rate
839 of flux emergence for emerging events with fluxes in the range $10^{16} - 10^{19}$ Mx.

840 By combining the distribution of emerged IN fluxes that we find here with the emergence
841 distributions observed by others for emerging events with fluxes greater than 10^{19} Mx we
842 find that flux emergence events of all sizes on the Sun follow a single power-law with a slope
843 of -2.69 . This implies a flux emergence rate of ≈ 450 Mx cm⁻² day⁻¹ from all emerging
844 events (from intranetwork ephemeral regions to sunspots) with more than 10^{16} Mx. This
845 rate is found to be dominated by flux from small-scale features and thus may be considered
846 approximately constant over the whole solar cycle. The suggestion that small-scale events
847 carry the dominant amount of flux into the photosphere is not new and agrees with the ideas
848 presented by various other authors including Socas-Navarro and Sánchez Almeida (2002).

849
850

6.1. Implications for the Generation and Surface Processing of Magnetic Flux

Recently, Parnell *et al.* (2009) established that the flux distribution of all magnetic features in the solar photosphere, at any instant, follows a power law with a slope of -1.85 , from the smallest observed features with fluxes of just 10^{16} Mx up to the largest sunspots with fluxes of 10^{23} Mx. The features investigated in their study were not newly emerged features, but simply all features of all sizes found in the photosphere at a particular instant in time. Physically a power-law distribution of flux implies that the fluxes are produced by a mechanism that is scale free. That is, the physical process(es) that produce the smallest magnetic features is (are) the same as the process(es) that produce all other features, including the largest features. Parnell *et al.* (2009) speculated that the distribution of magnetic feature fluxes was produced by one of two mechanisms. Either *i*) all magnetic features are created by a solar dynamo that acts in the same way on all scales or *ii*) magnetic features are created by dynamo action that is not the same on all scales; but, after emergence into the solar atmosphere, surface processes (*e.g.* fragmentation, coalescence and cancellation) dominate and create a single distribution of feature fluxes. In order to distinguish between these two mechanisms, it is obviously essential to determine whether the distribution of fluxes of newly emerged features follows a power law or not.

The work that we have presented here strongly suggests that the distribution of fluxes from all newly emerged features follows a power law which has a slope of ≈ 2.7 . This provides considerable support for the first mechanism, namely that all magnetic features are created by a solar dynamo that acts in the same way on all scales.

For more than five decades it has been known that the Sun's magnetic field is created by dynamo action occurring in or just below the convection zone (Parker, 1955, 1979; Moffatt, 1978; Choudhuri, 1998; Dikpati and Gilman, 2006; Weiss and Thompson, 2009). Theoretical modelling has established that a dynamo acting throughout the convection zone cannot produce sunspots, since magnetic buoyancy causes these strong magnetic fields to rise too rapidly (Parker, 1984; Choudhuri and Gilman, 1987). Instead, the generally accepted view is that these features are most likely created by a dynamo situated around the base of the convection zone (Spiegel and Weiss, 1980; Parker, 1993). This idea was strengthened by the discovery of the tachocline, a shear layer just below the base of the convection zone (Christensen-Dalsgaard and Schou, 1988; Schou, 1991; Parker, 1993; Schou *et al.*, 1998; Hughes, Rosner, and Weiss, 2007). Also, it has been suggested that small-scale emerging magnetic features are generated by a second (local) dynamo just below the photosphere (Cattaneo, 1999; Cattaneo and Hughes, 2001; Hagenaar, 2001). In this scenario, dynamo action is predominantly driven by turbulent convection flows, although the tachocline may play a role (Corbard and Thompson, 2002).

This picture of two separate dynamos dominating the flux distribution, one in the tachocline and one at the surface, is, however, inconsistent with our discovery of a single power-law over all emerging flux scales. Instead, as discussed in Parnell *et al.* (2009), it suggests that, in addition to the solar-cycle dynamo at the tachocline, turbulent dynamo action occurs continuously over a range of scales throughout the convection zone, from the tachocline right up to the surface. Parnell *et al.* (2009) found from their distributions of all photospheric feature fluxes that the numbers of the largest-scale flux features ($>10^{20}$ Mx) fall off at solar minimum. So they suggested that these large magnetic features are created in the tachocline, and the smaller features ($<10^{20}$ Mx) would continue to be produced in the convection zone throughout solar maximum and solar minimum. This idea has some support from the recent numerical convection simulations of Stein *et al.* (2008) and Nordlund (2008), which show that convection does not occur at two discrete scales (granulation

Small-Scale Flux Emergence Observed Using *Hinode*/SOT

and supergranulation), but rather that it occurs at a continuum of scales whose scale-length increases with depth.

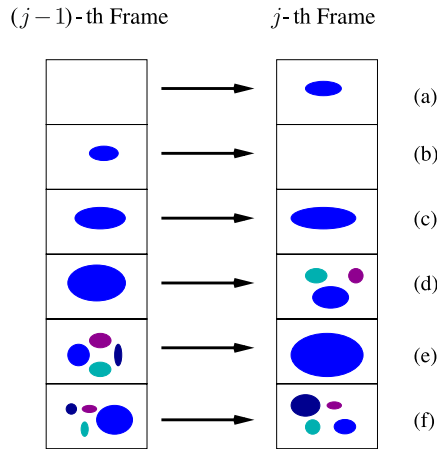
Furthermore, since the slope of our power-law is less than -2 , the global flux emergence rate appears, therefore, to be independent of the solar cycle with with a few times 10^{25} Mx injected per day from all emergence events with fluxes greater than 10^{16} Mx. This suggests that the dynamo that generates small-scale features with fluxes less than 10^{20} Mx (the turbulent dynamo throughout the convection zone) generates considerably more flux than the tachocline dynamo that creates active regions. Indeed, Schrijver and Harvey (1994) estimated that the total flux emerged in active regions over a typical 11-year solar cycle is of order 10^{25} Mx, whereas over the same period Schrijver *et al.* (1997) estimated that more than 10^{26} Mx are emerged via ephemeral regions (with fluxes of 10^{18} Mx or more). From our results we estimate that over a typical solar cycle some 2×10^{26} Mx are emerged in active regions with fluxes between 10^{20} – a few times 10^{22} Mx and 4.7×10^{27} Mx are emerged in ephemeral regions with fluxes between 10^{18} – 10^{20} Mx. Overall though, more than 10^{29} Mx are emerged in regions with fluxes $\geq 10^{16}$ Mx over a solar cycle. Some of the small-scale emerged flux may come from the recycling of active-region flux although, since there were many features on the Sun during the last very quiet minimum, it is clear that many small bipoles emerge even when there is no active region flux to recycle. If this is true it suggests that understanding how a dynamo generates small-scale magnetic features throughout the solar cycle is as important as understanding the generation mechanism of large-scale magnetic features.

Our observed slope of the distribution of newly emerged feature fluxes is steeper, ≈ 2.7 , than that of the general feature fluxes, -1.85 (Parnell *et al.*, 2009), *i.e.* there are fewer small-scale features at any instant in the solar photosphere than are found to emerge into the photosphere each day. There are likely to be two reasons for this. First, the short life times of small-scale features in comparison to large-scale features means that at any instant there is a good chance that most of the large-scale features will be counted, but many of the short-lived, small-scale ones will not be counted as they will no longer exist. Second, it suggests that coalescence of flux features could be the dominant surface process for small-scale features. This is not a surprise, as it is well known that small-scale features are swept to the edges and corners of supergranule cells where they coalesce.

The emerging flux results that we present in this paper are not conclusive proof of a scale-free dynamo, but they are highly suggestive of it. Clearly, the results plotted in Figure 11 have a reasonable spread and do not lie perfectly on a single line. The reasons for this are that the results plotted in the graph were all found using slightly different approaches, from different data sets with different spatial and temporal resolutions and different sensitivities. Furthermore, large-scale, and therefore invariably long-lived, emergence is relatively simple to detect and quantify, whilst small-scale, short-lived emergence is much more difficult to quantify, as discussed in this paper. In order to firmly establish the existence of a scale-free dynamo requires further work on both the theoretical and observational fronts. In particular, to find the slope of the resulting flux distribution to a high degree of accuracy from observations requires an approach that determines the fluxes of all newly emerged features on all scales in a consistent manner.

Acknowledgements LMT acknowledges the support of STFC during her PhD, whilst CEP acknowledges support from the Phillip Leverhulme Trust by way of a Leverhulme prize and from STFC as part of the Solar and Magnetospheric Theory Group's Rolling Grant. This work benefited from the preparation of data undertaken as part of the Magnetic Tracking Workshop series, which is enabled in part by funding from NASA's SHP Guest Investigator program. *Hinode* is a Japanese mission developed and launched by ISAS/JAXA, with NAOJ as domestic partner and NASA and STFC (UK) as international partners. It is operated by these agencies in cooperation with ESA and NSC (Norway).

951 **Figure 12** An illustration of the
 952 various cases which can occur
 953 when associating features
 954 between frames: (a) none to one,
 955 (b) one to none, (c) one to one,
 956 (d) one to many, (e) many to one
 957 and (f) many to many.



967 **Appendix A: Feature Tracking**

968
 969 Feature tracking involves associating a feature in one frame with a like-polarity feature
 970 in the previous frame. This enables individual flux features to be tracked in time so that
 971 their lifetimes, peak fluxes and peak areas can be calculated. Feature tracking would be
 972 straight forward if features overlapped at most one feature in the previous frame. However,
 973 complications arise because multiple like-polarity features often overlap between frames, as
 974 illustrated in Figure 12. For instance, the processes of fragmentation and coalescence lead to
 975 a ‘one to many’ overlap and a ‘many to one’ overlap, respectively. It is also possible to find
 976 ‘many to many’ overlaps of features which arise through a combination of these processes.
 977 Below we describe how we associate features in each case.

978 **A.1. Associating Features Between Frames**

979
 980 We consider each pair of consecutive frames in turn to associate the like-polarity features
 981 between frames. In order for two like-polarity features to be associated they must overlap
 982 and have comparable flux. We look at each feature Φ_k^j in frame j and compare the pixels
 983 it involves with the corresponding pixels in frame $j - 1$. Similarly, we also compare all the
 984 pixels of feature Φ_i^{j-1} with the corresponding pixels in frame j . All cases which arise are
 985 described below.

- 986 • **None to one:** If Φ_k^j does not overlap any like-polarity features in frame $j - 1$, Φ_k^j is said
 987 to have ‘appeared’ and is given a new unique label.
- 988 • **One to none:** If Φ_i^{j-1} does not overlap any like-polarity features in frame j , it is said to
 989 have ‘disappeared’ and it’s unique label is not used again after frame $j - 1$.
- 990 • **One to one:** If there is a unique overlap between like-polarity features Φ_i^{j-1} and Φ_k^j , then
 991 Φ_k^j is given the unique label of Φ_i^{j-1} and the feature is flagged as ‘pre-existing’.
- 992 • **One to many:** If Φ_i^{j-1} overlaps m like-polarity features ($\Phi_{k1}^j, \dots, \Phi_{km}^j$) in frame j , the
 993 unique label of Φ_i^{j-1} will be passed on to the feature in j which satisfies the following
 994 conditions. Let feature $\Phi_{k\alpha}^j$ ($\alpha \in 1, \dots, m$) overlap Φ_i^{j-1} with an area of $a_{ik\alpha}^{j-1}$. The total
 995 area of overlap with all features $\Phi_{k\alpha}^j$ is

$$\sum_{\alpha=1}^m a_{ik\alpha}^{j-1} \leq A_i^{j-1},$$

Small-Scale Flux Emergence Observed Using *Hinode*/SOT

where A_i^{j-1} is the area of the feature Φ_i^{j-1} . The ‘ \leq ’ arises since it is possible that some of the pixels of Φ_i^{j-1} may not overlay anything in frame j . All features $\Phi_{k\alpha}^j$ with

$$a_{ik\alpha}^{j-1} \geq \frac{A_i^{j-1}}{m}$$

are potential candidates for taking the unique label of Φ_i^{j-1} . If there is only one feature which satisfies this condition, it automatically takes the Φ_i^{j-1} label. If there are several features then the feature $\Phi_{k\alpha}^j$, whose flux $\Psi_{k\alpha}^j$ is closest to the flux Ψ_i^{j-1} of Φ_i^{j-1} , is taken. All other features in frame j are flagged as having ‘appeared through fragmentation’ and they are all given new unique labels.

- **Many to one:** If n like-polarity features in frame $j - 1$ ($\Phi_{i1}^{j-1}, \dots, \Phi_{in}^{j-1}$) overlap a single feature Φ_k^j in frame j , then Φ_k^j will receive the unique label of the feature which satisfies the following conditions. In a similar manner to the one-to-many case, feature $\Phi_{i\alpha}^{j-1}$ ($\alpha \in 1, \dots, n$) overlaps Φ_k^j with an area of $a_{ki\alpha}^j$ such that the total area of overlap with all features is

$$\sum_{\alpha=1}^n a_{ki\alpha}^j \leq A_k^j,$$

where A_k^j is the area of the feature Φ_k^j . As above, all features $\Phi_{i\alpha}^{j-1}$ with

$$a_{ki\alpha}^j \geq \frac{A_k^j}{n}$$

are potential candidates for passing on their unique labels to Φ_k^j . If there is only one such feature $\Phi_{i\alpha}^{j-1}$ then this feature gives its unique label to Φ_k^j . If there is more than one feature, then the feature $\Phi_{i\alpha}^{j-1}$ whose flux $\Psi_{i\alpha}^{j-1}$ is closest to the flux Ψ_k^j of Φ_k^j passes on its label. All the other $\Phi_{i\alpha}^{j-1}$ features are flagged as having ‘disappeared through merging’.

- **Many to many:** If n like-polarity features in frame $j - 1$ ($\Phi_{i1}^{j-1}, \dots, \Phi_{in}^{j-1}$) overlap with m features in frame j ($\Phi_{k1}^j, \dots, \Phi_{km}^j$), then several labels can be carried forward from frame $j - 1$ to frame j . To determine which features are associated between frames, we combine the rules used in the one-to-many and many-to-one cases. All feature pairings $\Phi_{i\alpha}^{j-1}$ ($\alpha \in 1, \dots, n$) and $\Phi_{k\beta}^j$ ($\beta \in 1, \dots, m$) which satisfy the following overlapping and flux ratio rules are potential candidates for association:

$$a_{i\alpha k\beta}^{j-1} \geq \frac{A_{i\alpha}^{j-1}}{m} \quad \text{and} \quad a_{k\beta i\alpha}^j \geq \frac{A_{k\beta}^j}{n},$$

where $a_{i\alpha k\beta}^{j-1}$ is the area by which $\Phi_{k\beta}^j$ overlaps $\Phi_{i\alpha}^{j-1}$, which has area $A_{i\alpha}^{j-1}$ and, similarly, $a_{k\beta i\alpha}^j$ is the area by which $\Phi_{i\alpha}^{j-1}$ overlaps $\Phi_{k\beta}^j$, which has area $A_{k\beta}^j$. Furthermore, in all situations that the above criteria do not yield unique associations, the further constraint that the ratio of the fluxes of the features, $\Psi_{i\alpha}^{j-1} / \Psi_{k\beta}^j$, is closest to one is applied. Once unique associations have been established the labels from the $\Phi_{i\alpha}^{j-1}$ features are transferred to the $\Phi_{k\beta}^j$ features where appropriate. Features from frame $j - 1$ which are not associated are flagged as ‘disappeared through merging’ and the features from frame j which are not associated are flagged as ‘appeared through fragmentation’ and given new unique labels.

1051 Once every pair of frames has been considered the association process is complete and
1052 each tracked feature will have a unique label, which remains with it for its entire life. This
1053 means that the frame of birth and death of all tracked features can easily be determined from
1054 the frames in which a feature's unique label first appears or finally disappears, respectively.

1055 As noted earlier, further data filtering is applied at this stage, with the removal of all
1056 features whose lifetime is less than four frames (6 min). This reduces the risk of counting
1057 spurious fluctuations in the data as features.

1058
1059

1060 **Appendix B: Description of Bipole Comparison Method**

1061

1062 In the Bipole Comparison Method, the identification of flux emergence events is undertaken
1063 in three steps using untracked features. In step one, we find opposite-polarity bipoles in the
1064 individual frames (Section B.1). In the second step, we determine which bipoles are newly
1065 emerged (Section B.2) and then, in the final step, we select which of these bipoles are unique
1066 (Section B.3).

1067

1068 B.1. Bipole Identification

1069

1070 In frame j , the i th opposite-polarity pair of features consists of a positive feature Φ_{i+}^j with
1071 flux Ψ_{i+}^j and a negative feature Φ_{i-}^j with flux Ψ_{i-}^j . We define Δ as the shortest distance
1072 between the boundaries of Φ_{i+}^j and Φ_{i-}^j . This pair of features is defined as a bipole if $\Delta \leq$
1073 $\Delta_0 = 7$ pixels ≈ 0.8 Mm and the ratio of the fluxes of the features satisfies

1074

$$1075 \frac{1}{\rho} \leq \frac{|\Psi_{i+}|}{|\Psi_{i-}|} \leq \rho,$$

1076

1077 where $\rho = 3$.

1078

1079 The value $\Delta_0 = 7$ was chosen for the following reasons. *i)* A visual inspection of the
1080 feature results reveals that they have equivalent areas and fluxes to intranetwork features,
1081 which are known to emerge on scales of less than 1 Mm (*e.g.* Strous and Zwaan, 1999).
1082 *ii)* After running trials using values of Δ_0 between five and nine pixels, we found that $\Delta_0 = 7$
1083 pixels gave the most reasonable pairings according to visual inspection (*e.g.*, a separation of
1084 just five pixels appeared to miss a number of obvious emerging pairs, whilst a separation of
1085 nine pixels paired too many features).

1086

1087 The value of three for ρ was chosen following trials involving values of ρ between one
1088 and five. Manual inspection of the data revealed that values of ρ close to one led to many
1089 bipoles being discounted and ρ too large (near five) led to the pairing of features which a
1090 visual inspection suggested were not connected. Ideally one would expect the features of
1091 a true bipole to contain equal amounts of flux, but this is rarely the case as imbalances of
1092 flux often arise. These can arise for several reasons, for instance, features in a bipole can
1093 coalesce and fragment from birth (Martin, 1988), noise in the data, although minimised in
1094 the preparation of the data, may result in fluctuations of a feature's flux and if all the flux
1095 in both features of the bipole is not completely vertical, the line-of-sight flux in one feature
1096 may register much lower than that of the other feature.

1097

1098 B.2. Finding Emerging Bipoles

1099

1098 The next step is to determine which of the identified bipoles are newly emerged. The data
1099 array is split into a positive polarity array and a negative polarity array, for each frame j .

1100

Small-Scale Flux Emergence Observed Using *Hinode*/SOT

1101 All features which are deemed to be part of a bipolar pair are then dilated by three pixels
 1102 in each frame, producing new features $D\Phi_{i+}^j$ and $D\Phi_{i-}^j$. Each feature is dilated to take into
 1103 account that it can move, fragment or coalesce between frames. A dilation of three pixels
 1104 (348 km), corresponding to a separation of two pixels, is chosen on the basis that features
 1105 move with a velocity of $\approx 2 \text{ km s}^{-1}$ (de Wijn *et al.*, 2008), so within 90 s (the cadence of
 1106 the data) the features move roughly 180 km. The pixels of each $D\Phi_i^j$ are then compared
 1107 with the corresponding pixels in the $j - 1$ frame for the undilated features. Four possible
 1108 situations arise.

- 1109 *i*) Feature $D\Phi_i^j$ overlaps no like-polarity features in the $j - 1$ frame. In this case Φ_i^j is
 1110 flagged as **emerging**.
 1111 *ii*) If $D\Phi_i^j$ overlaps n like-polarity features in the $j - 1$ frame, then the undilated flux Ψ_i^j is
 1112 compared to the fluxes Ψ_k^{j-1} ($k \in 1, \dots, n$) of the n features it overlaps in frame $j - 1$.
 1113 One of three cases may arise
 1114 (a) If the flux Ψ_i^j satisfies

1115
 1116
 1117
$$\sum_{k=0}^n |\Psi_k^{j-1}| \ll \frac{|\Psi_i^j|}{\rho_k},$$

 1118

1119 then the feature Φ_i^j is flagged as **emerging** (*i.e.*, the flux Ψ_i^j of the feature in frame
 1120 j must be significantly bigger than the sum of the fluxes of the features it overlaps
 1121 in frame $j - 1$). The value of ρ_k used is the same as the value used for ρ above,
 1122 hence, $\rho_k = 3$.
 1123

- 1124 (b) If the flux of Φ_i^j satisfies

1125
 1126
$$\frac{|\Psi_i^j|}{\rho_k} < \sum_{k=0}^n |\Psi_k^{j-1}| < |\Psi_i^j|,$$

 1127
 1128

1129 then the feature is flagged as **increasing**, since its growth between frames is not
 1130 significant.

- 1131 (c) If the flux of Φ_i^j satisfies

1132
 1133
$$\sum_{k=0}^n |\Psi_k^{j-1}| > |\Psi_i^j|,$$

 1134
 1135

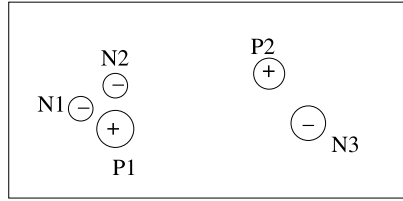
1136 then the feature is flagged as **decreasing**, since its flux has decreased between
 1137 frames.

1138 To be an emerging pair the bipole Φ_{i+}^j and Φ_{i-}^j must comprise of either two features that
 1139 are flagged as emerging or one emerging feature and one increasing feature.

1140
 1141 B.3. Selecting Unique Bipoles
 1142

1143 Once all the emerging bipolar pairs were identified it was found that many of them did not
 1144 constitute unique pairings. This occurred for two main reasons. Firstly, if a true bi-
 1145 pole coincidentally emerged close to other appearing features, its features may be paired
 1146 with one or more of these other features, whether they are genuine emergences or not. Sec-
 1147 ondly, if a cluster of positive and a cluster of negative features emerge together, due, for
 1148 instance, to a bipole being shredded by convection as it is rising through the convection
 1149 zone, then this could again lead to the multiple pairings of features. The aim of this step is to
 1150

1151 **Figure 13** A cartoon of a
 1152 magnetogram with two emerging
 1153 events. The event on the left
 1154 shows non-unique pairings whilst
 1155 the one on the right is a simple
 1156 bipole.
 1157
 1158
 1159



1160 identify which non-unique pairings are due to coincidental nearby appearances and which
 1161 are due to cluster-like emergence.

1162 A cluster-like emergence can involve clusters of features of both polarities that all emerge
 1163 together or it may involve a lone feature of one polarity emerging with a cluster of features
 1164 of the opposite polarity. To find out if there are any clusters of same-sign flux appearing
 1165 together, we take all the newly emerged features in each frame and dilate them by three
 1166 pixels. Then, by considering each dilated feature in turn, like-polarity overlapping emerging
 1167 neighbours are identified. If an emerging feature has a like-polarity emerging neighbour
 1168 these features are said to be associated. We are interested in finding all the third party like-
 1169 polarity associations in order that we can identify like-polarity clusters of features. In order
 1170 to do this we utilise an association matrix (Close *et al.*, 2005; Close, Parnell, and Priest,
 1171 2005).

1172 If there are N like-polarity features in a frame, then the initial association matrix, Assoc_0 ,
 1173 will be an $N \times N$ matrix. If a feature i is associated with a feature k then $\text{Assoc}_0(i, k) = 1$,
 1174 else $\text{Assoc}_0(i, k) = 0$. Clearly, the matrix will be symmetric, since association is commu-
 1175 tative. Furthermore, all features are assumed to be associated with themselves and so the
 1176 diagonal elements of the matrix are non-zero, $\text{Assoc}_0(i, i) = 1$.

1177 Figure 13 shows a cartoon of an example magnetogram in which three bipolar pairs have
 1178 been identified, P1 – N1, P1 – N2, P2 – N3. The initial association matrix for this example is

1179
 1180
 1181
 1182
 1183
 1184
 1185

$$\text{Assoc}_0 = \begin{matrix} & \begin{matrix} \text{P1} & \text{P2} & \text{N1} & \text{N2} & \text{N3} \end{matrix} \\ \begin{matrix} \text{P1} \\ \text{P2} \\ \text{N1} \\ \text{N2} \\ \text{N3} \end{matrix} & \begin{pmatrix} 1 & 0 & 1 & 1 & 0 \\ 0 & 1 & 0 & 0 & 1 \\ 1 & 0 & 1 & 0 & 0 \\ 1 & 0 & 0 & 1 & 0 \\ 0 & 1 & 0 & 0 & 1 \end{pmatrix} \end{matrix}.$$

1186 To identify clusters of associated features we need to find all the third party associations.
 1187 This is simply achieved by repeated multiplication of the association matrix by itself,
 1188

1189
 1190

$$\text{Assoc}_n = \text{Assoc}_{n-1} \times \text{Assoc}_{n-1} \quad n \geq 1,$$

1191 where all non-zero values of Assoc_n are fixed at each step to one. This step is repeated until
 1192 the entries of Assoc_n no longer change, *i.e.* until
 1193

1194
 1195
 1196
 1197

$$\sum_{i,j=1}^N \text{Assoc}_n(i, k) = \sum_{i,j=1}^N \text{Assoc}_{n-1}(i, k).$$

1198 The non-zero entries of the i th row of the final matrix can then be simply read off to reveal
 1199 all the features which belong to the cluster that involves the i th feature.
 1200

Small-Scale Flux Emergence Observed Using *Hinode/SOT*

1201 We then consider in turn all the non-unique bipoles and investigate the associations of all
 1202 their like-polarity features. Non-unique bipoles containing features which are deemed to be
 1203 part of a cluster are kept.

1204 If we follow these steps for our example then the association matrix converges very
 1205 quickly:

1206
 1207
 1208
 1209
 1210
 1211
 1212

$$\text{Assoc}_2 = \text{Assoc}_1 = \begin{matrix} & \text{P1} & \text{P2} & \text{N1} & \text{N2} & \text{N3} \\ \text{P1} & \left(\begin{matrix} 1 & 0 & 1 & 1 & 0 \\ 0 & 1 & 0 & 0 & 1 \\ 1 & 0 & 1 & 1 & 0 \\ 1 & 0 & 1 & 1 & 0 \\ 0 & 1 & 0 & 0 & 1 \end{matrix} \right) \\ \text{P2} \\ \text{N1} \\ \text{N2} \\ \text{N3} \end{matrix}.$$

1213 Thus, for example, we see that our association matrix reveals that the two negative features
 1214 N1 and N2 are associated and they share a common positive feature P1. Therefore, the two
 1215 bipoles containing features P1, N1 and N2 are deemed to form a cluster emergence.

1216 For the remaining non-unique pairings which are not found to be involved in cluster
 1217 emergences, the flux ratios of the features in each bipolar pair are considered and the bipole
 1218 with the ratio closest to unity is regarded as the true emerging bipole and is retained. The
 1219 other bipoles are removed.

1222 **Appendix C: Description of Tracked Bipolar Emergence**

1223
 1224 In the BC method, bipoles are identified in each frame, but they are not associated between
 1225 frames, so it is not possible to follow their evolution. The tracked bipole method is very
 1226 similar to the BC method except that it is applied to the tracked data. Indeed, the first and
 1227 last steps of this method are the same as that used in the BC method, but the second step is
 1228 different.

1230 **C.1. Identifying Bipolar Emergence**

1231
 1232 In order to identify emerging bipoles, bipolar pairs of features Φ_{i+}^j and Φ_{i-}^j identified in
 1233 the tracked data are required. These are found using the method described in Section B.1.
 1234 To find which of these bipoles are actually emerging bipoles we use the ‘birth’ information
 1235 obtained in Appendix A. To be classed as an emergence both features of a bipolar pair must
 1236 be born within ten frames (15 min) of each other and, at their birth, they must have both
 1237 been flagged as ‘appeared’ or one feature must have been flagged as ‘appeared’ and the
 1238 other flagged as ‘appeared through fragmentation’.

1239 As in the previous method, many of these emerging bipoles do not constitute unique
 1240 pairings, so we use the approach of Section B.3 to determine which non-unique pairs form
 1241 cluster emergences, and can be retained, and which should be removed.

1244 **Appendix D: Tracked Cluster Emergence**

1245
 1246 The tracked cluster method is designed to identify emerging clusters of features from a
 1247 tracked data set (*i.e.*, emerging events that involve more than two features of opposite polar-
 1248 ity). The approach applied here is quite different from the two previous methods, although
 1249 it also involves three stages.

1250

D.1. Identifying Feature Emergence

Using the tracked features, we flag, in each frame, features which have ‘recently appeared’. A feature Φ_i^j is said to have ‘recently appeared’ if the following holds.

1. It was born by ‘appearing’ or ‘appearing through fragmentation’ sometime within the previous ten frames (15 min).
2. If it is flagged as ‘appeared through fragmentation’ then the feature Φ_k^s from which it fragmented must be flagged as ‘recently appeared’ and $j - 10 \leq s \leq j$.
3. Its flux Ψ_i^j is initially small: $|\Psi_i^j| \leq \alpha$, where α is taken to be 2.7×10^{17} Mx ($\frac{1}{3}$ of all feature fluxes are below this value).
4. Its area A_i^j is initially small: $A_i^j \leq \beta$, where β is taken to be 0.3 Mm^2 ($\frac{1}{3}$ of all feature areas are below this value).

All features that satisfy the above criteria are retained for the next stage of the analysis, which involves finding opposite-polarity associations.

D.2. Finding Like-Polarity Clusters

To find recently-appeared like-polarity clusters, all recently-appeared features within a given frame are dilated by three pixels to see if they have any like-polarity neighbours. Clusters are then identified by creating an association matrix, as described in Section B.3. Note that this stage does not remove any like-polarity features, it simply identifies clusters. If a recently appeared feature has no like-polarity neighbours it is still retained.

D.3. Finding Opposite-Polarity Associations

Unlike the other two methods which start off by identifying features which have opposite-polarity neighbours we leave this until the final step of this method. In order to identify if our recently-appeared features are part of an emerging event we dilate all the features of each recently appeared like-polarity cluster or lone feature in frame j by eight pixels (as used in the tracked bipolar method Section C.1). The pixels of the dilated cluster or lone feature in frame j are then compared with the same pixels in frames $j - 2$, $j - 1$, $j + 1$ and $j + 2$ to see if they contain any of the recently-appeared features of opposite-polarity. An emerging event is defined as a ‘recently appeared’ lone tracked feature or like-polarity cluster of tracked features that has at least one association to either an opposite-polarity lone tracked feature or a cluster of opposite-polarity tracked features.

References

- Cattaneo, F.: 1999, *Astrophys. J. Lett.* **515**, 39.
Cattaneo, F., Hughes, D.W.: 2001, *Astron. Geophys.* **42**, 318.
Chae, J., Wang, H., Qiu, J., Goode, P.R., Strous, L., Yun, H.S.: 2001, *Astrophys. J.* **548**, 497.
Choudhuri, A.R.: 1998, *Physics of Fluids and Plasmas*, Cambridge University Press, Cambridge, 340.
Choudhuri, A.R., Gilman, P.A.: 1987, *Astrophys. J.* **316**, 788.
Christensen-Dalsgaard, J., Schou, J.: 1988, In: Rolfe, E. (ed.) *Seismology of the Sun and Sun-Like Stars SP-286*, ESA, Noordwijk, 149.
Close, R.M., Parnell, C.E., Priest, E.R.: 2005, *Geophys. Astrophys. Fluid Dyn.* **99**, 513.
Close, R.M., Parnell, C.E., Longcope, D.W., Priest, E.R.: 2005, *Solar Phys.* **231**, 45.
Corbard, T., Thompson, M.J.: 2002, *Solar Phys.* **205**, 211.
de Wijn, A.G., Lites, B.W., Berger, T.E., Frank, Z.A., Tarbell, T.D., Ishikawa, R.: 2008, *Astrophys. J.* **684**, 1469.

Small-Scale Flux Emergence Observed Using *Hinode*/SOT

- 1301 DeForest, C.E.: 1998, 'ZTOOLS'. Software package distributed via SolarSoft.
- 1302 DeForest, C.E., Hagenaar, H.J., Lamb, D.A., Parnell, C.E., Welsch, B.T.: 2007, *Astrophys. J.* **666**, 576.
- 1303 Dikpati, M., Gilman, P.A.: 2006, *Astrophys. J.* **649**, 498.
- 1304 Domínguez Cerdeña, I., Sánchez Almeida, J., Kneer, F.: 2006, *Astrophys. J.* **636**, 496.
- 1305 Hagenaar, H.J.: 2001, *Astrophys. J.* **555**, 448.
- 1306 Hagenaar, H.J., Schrijver, C.J., Title, A.M.: 2003, *Astrophys. J.* **584**, 1107.
- 1307 Hagenaar, H.J., DeRosa, M.L., Schrijver, C.J.: 2008, *Astrophys. J.* **678**, 541.
- 1308 Harvey, K.L., Schrijver, C.J., Title, A.M., Shine, R.A.: 1999, *Astrophys. J.* **511**, 932.
- 1309 Harvey, K.L.: 1993, Magnetic bipoles on the Sun. Ph.D. Thesis, University of Utrecht.
- 1310 Harvey, K.L., Martin, S.F.: 1973, *Solar Phys.* **32**, 389.
- 1311 Harvey, K.L., Zwaan, C.: 1993, *Solar Phys.* **148**, 85.
- 1312 Harvey, J.W., Harvey, K.L., Martin, S.F.: 1975, *Solar Phys.* **40**, 87.
- 1313 Harvey, K.L., Harrison, J.P., Schrijver, C.J., Penn, M.J.: 1999, *Solar Phys.* **397**, 51.
- 1314 Harvey, J.W., Branston, D., Henney, C.J., Keller, C.U.: 2007, *Astrophys. J. Lett.* **659**, 177.
- 1315 Hughes, D.W., Rosner, R., Weiss, N.O.: 2007, *The Solar Tachocline*, Cambridge University Press, Cambridge, Chapter 1.
- 1316 Ichimoto, K., Katsukawa, Y., Tarbell, T., Shine, R.A., Hoffmann, C., Berger, T., et al.: 2008, In: Matthews, S.A., Davis, J.M., Harra, L.K. (eds.) *First Results From Hinode CS-397*, Astron. Soc. Pac., San Francisco, 5.
- 1317 Keller, C.U., Deubner, F.L., Egger, U., Fleck, B., Povel, H.P.: 1994, *Astron. Astrophys.* **286**, 626.
- 1318 Khomenko, E.V., Martínez González, M.J., Collados, M., Vögler, A., Solanki, S.K., Ruiz Cobo, B., Beck, C.: 2005, *Astron. Astrophys.* **436**, L27.
- 1319 Kosugi, T., Matsuzaki, K., Sakao, T., Shimizu, T., Sone, Y., Tachikawa, S., et al.: 2007, *Solar Phys.* **243**, 3.
- 1320 Lamb, D.A., DeForest, C.E., Hagenaar, H.J., Parnell, C.E., Welsch, B.T.: 2008, *Astrophys. J.* **674**, 520.
- 1321 Lamb, D.A., DeForest, C.E., Hagenaar, H.J., Parnell, C.E., Welsch, B.T.: 2010, *Astrophys. J.* **720**, 1405.
- 1322 Lin, H., Rimmele, T.: 1999, *Astrophys. J.* **514**, 448.
- 1323 Lites, B.W., Kubo, M., Socas-Navarro, H., Berger, T., Frank, Z., Shine, R., et al.: 2008, *Astrophys. J.* **672**, 1237.
- 1324 Livi, S.H., Wang, J., Martin, S.F.: 1985, *Aust. J. Phys.* **38**, 855.
- 1325 Livingston, W.C., Harvey, J.W.: 1975, *Bull. Am. Astron. Soc.* **7**, 346.
- 1326 Manso Sainz, R., Landi Degl'Innocenti, E., Trujillo Beuno, J.: 2004, *Astrophys. J. Lett.* **614**, 89.
- 1327 Martin, S.F.: 1988, *Solar Phys.* **117**, 243.
- 1328 Martínez González, M.J., Bellot Rubio, L.R.: 2009, *Astrophys. J.* **700**, 1391.
- 1329 Moffatt, H.K.: 1978, *Magnetic Field Generation in Electrically Conducting Fluids*, Cambridge University Press, Cambridge, Chapter 5.
- 1330 Nordlund, A.: 2008, *Phys. Scr.* **133**, 014002.
- 1331 Orozco Suárez, D., Bellot Rubio, L.R., del Toro Iniesta, J.C., Tsuneta, S.: 2008, *Astron. Astrophys. Lett.* **481**, 33.
- 1332 Parker, E.N.: 1955, *Astrophys. J.* **122**, 293.
- 1333 Parker, E.N.: 1979, *Cosmical Magnetic Fields: Their Origin and Their Activity*, Clarendon Press, Oxford, Chapter 21.
- 1334 Parker, E.N.: 1984, *Astrophys. J.* **281**, 839.
- 1335 Parker, E.N.: 1993, *Astrophys. J.* **408**, 707.
- 1336 Parnell, C.E.: 2001, *Solar Phys.* **200**, 23.
- 1337 Parnell, C.E.: 2002, *Mon. Not. Roy. Astron. Soc.* **335**, 389.
- 1338 Parnell, C.E., DeForest, C.E., Hagenaar, H.J., Lamb, D.A., Welsch, B.T.: 2008, In: Matthews, S.A., Davis, J.M., Harra, L.K. (eds.) *First Results From Hinode CS-397*, Astron. Soc. Pac., San Francisco, 31.
- 1339 Parnell, C.E., DeForest, C.E., Hagenaar, H.J., Johnston, B.A., Lamb, D.A., Welsch, B.T.: 2009, *Astrophys. J.* **698**, 75.
- 1340 Rezaei, R.: 2007, *Astron. Astrophys. Lett.* **476**, 33.
- 1341 Sánchez Almeida, J.: 2007, *Astrophys. J.* **657**, 1150.
- 1342 Sánchez Almeida, J., Emonet, T., Cattaneo, F.: 2003, *Astrophys. J.* **585**, 536.
- 1343 Schou, J.: 1991, In: Gough, D., Toomre, J. (eds.) *Challenges to Theories of the Structure of Moderate-Mass Stars*, Springer Lecture Notes in Physics **388**, 81.
- 1344 Schou, J., Antia, H.M., Basu, S., Bogart, R.S., Bush, R.I., Chitre, S.M., et al.: 1998, *Astrophys. J.* **505**, 390.
- 1345 Schrijver, C.J., Harvey, K.L.: 1994, *Solar Phys.* **150**, 1.
- 1346 Schrijver, C.J., Title, A.M., van Ballegoolijen, A.A., Hagenaar, H.J., Shine, R.A.: 1997, *Astrophys. J.* **487**, 424.
- 1347 Smithson, R.C.: 1975, *Bull. Am. Astron. Soc.* **7**, 346.
- 1348 Socas-Navarro, H., Sánchez Almeida, J.: 2002, *Astrophys. J.* **565**, 1323.
- 1349 Socas-Navarro, H., Martínez Pillet, V., Lites, B.W.: 2004, *Astrophys. J.* **611**, 1139.
- 1350

- 1351 Spiegel, E.A., Weiss, N.O.: 1980, *Nature* **287**, 616.
1352 Stein, R.F., Nordlund, A., Georgobiani, D., Benson, D., Schaffenberger, W.: 2008, [arXiv:0811.0472](https://arxiv.org/abs/0811.0472).
1353 Strous, L.H., Zwaan, C.: 1999, *Astrophys. J.* **527**, 435.
1354 Title, A.: 2000, *Philos. Trans. Roy. Soc. London A* **358**, 657.
1355 Tsuneta, S., Ichimoto, K., Katsukawa, Y., Nagata, S., Otsubo, M., Shimizu, T., *et al.*: 2008, *Solar Phys.* **249**, 167.
1356 Wang, H.: 1988, *Solar Phys.* **116**, 1.
1357 Wang, J., Wang, H., Tang, F., Lee, J.W., Zirin, H.: 1995, *Solar Phys.* **160**, 277.
1358 Weiss, N.O., Thompson, M.J.: 2009, *Space Sci. Rev.* **144**, 53.
1359 Welsch, B.T., Longcope, D.W.: 2003, *Astrophys. J.* **588**, 620.
1360 Zirin, H.: 1985, *Aust. J. Phys.* **38**, 929.
1361 Zirin, H.: 1987, *Solar Phys.* **110**, 101.
1362 Zwaan, C.: 1985, *Solar Phys.* **100**, 397.

1363
1364
1365
1366
1367
1368
1369
1370
1371
1372
1373
1374
1375
1376
1377
1378
1379
1380
1381
1382
1383
1384
1385
1386
1387
1388
1389
1390
1391
1392
1393
1394
1395
1396
1397
1398
1399
1400